Geophysical Journal International

Geophys. J. Int. (2014) **196,** 493–509
Advance Access publication 2013 October 17

doi: 10.1093/gji/ggt384

Constraints on crustal attenuation and three-dimensional spatial distribution of stress drop in Switzerland

Bettina P. Goertz-Allmann[1,*] and Benjamin Edwards[2]

[1] *NORSAR, Kjeller, Norway. E-mail: bettina@norsar.no*
[2] *Swiss Seismological Service, ETH Zurich, Zurich, Switzerland*

Accepted 2013 September 19. Received 2013 August 12; in original form 2013 January 30

SUMMARY

We employ two different methods to estimate attenuation-corrected source spectra and calculate Brune stress drops of small to medium earthquakes in Switzerland and the surrounding region. We test trade-offs between source and travel path contributions by comparing results between a data-driven and a model-dependent method of distinguishing between the two. Systematic differences between results from both methods can best be reconciled by assuming intrinsic whole-path attenuation to be frequency dependent. A two-parameter grid search based on a power-law $Q(f)$ function reveals trade-offs that prevent us from quantifying a more exact frequency dependence. However, a comparison of the two-source parameter inversion methods with synthetic tests provide evidence for a non-negligible frequency dependence of Q between 1 and 30 Hz. Consideration of these implications on the attenuation model, as well as consideration of lateral and vertical variations of velocity and quality factor reduces the scatter of the obtained stress drop estimates. Synthetic tests confirm that both methods are able to robustly resolve lateral variations of Brune stress drop with quantifiable uncertainty estimates. Resulting lateral variations show reduced stress drop along the Alpine deformation front. This pattern points to tectonic causes and may be due to variations in differential stress.

Key words: Earthquake source observations; Seismicity and tectonics; Body waves; Seismic attenuation; Site effects.

1 INTRODUCTION

The determination of dynamic source parameters, such as stress drop, rupture duration or radiated seismic energy is important for two reasons: on one hand, dynamic source properties can reveal information about the state of stress and rheological properties of a seismogenic region. On the other hand, the systematic determination of these source properties can yield more fundamental information about the physical process of earthquake nucleation, as well as possible physical differences between small and large earthquakes.

The stress drop of an earthquake can be determined from the high-frequency fall-off of the source spectrum. The corner frequency of an ω^{-2} source model (Brune 1970, 1971) is related to the stress drop (e.g. Eshelby 1957) and can be estimated by least-squares fitting of an ω^{-2} source model to travel path corrected source spectra. The challenge of this approach is the separation of true source effects from attenuation effects along the travel path, which can affect the measured spectra in very similar ways. A traditional approach to this problem is the application of so-called empirical Green's function (EGF) corrections where the event to be evaluated is deconvolved with a smaller colocated event in order to get rid of travel path effects that both events have in common (see, e.g. Mueller 1985; Hough 1997). However, the smaller the events, the more difficult it becomes to find both well-recorded and sufficiently smaller events in close vicinity that are suitable for an EGF correction.

Alternative approaches to separate source from propagation path effects rely on the redundancy contained in multiple crossing travel paths sampled through large event catalogues recorded by large networks. Such approaches become especially effective for events below magnitude 3 (Shearer *et al.* 2006). The challenges of such methods are twofold: first, care has to be taken in checking the source–receiver geometry to detect and avoid possible bias through incomplete ray coverage. Secondly, directivity effects can have an impact on source spectra (Haskell 1964; Kane *et al.* 2013), and are difficult to separate since the rupture direction is *a priori* unknown. One typically assumes that directivity effects are averaged out by recording of a number of stations from a range of azimuths (Shearer *et al.* 2006; Allmann & Shearer 2007). Ide *et al.* (2003) argue for additional bias in source property determination introduced by correcting for a frequency-independent attenuation, and

*Formerly at: ETH Zurich, Switzerland.

they see evidence for frequency dependence of Q in deep borehole recordings.

A frequency-dependence of Q is often found in spectral inversion studies over local to regional distances (e.g. Castro *et al.* 1990; Drouet *et al.* 2008; Oth *et al.* 2011; McNamara *et al.* 2012). Even though they can be formulated in a non-parametric way, these methods require an *a priori* assumption for geometrical spreading (typically a spherical or hinged multilinear term), which may result in significant trade-offs in more heterogeneous regions. Other authors find either only little frequency dependence (e.g. Adams & Abercrombie 1998), or a depth dependence of Q to be the dominating factor (Hough & Anderson 1988; Abercrombie 2000; Edwards & Rietbrock 2009). Furthermore, borehole measurements typically find depth dependence of Q dominating over frequency dependence (e.g. Toverud & Ursin 2005; Blias 2012, and references therein). It is, however, difficult to resolve a depth dependence of Q from distance-dependent spectral inversion. Finally, despite many studies of source parameter inversions attempting to simultaneously determine, or predefine, the frequency dependence of Q, it has been repeatedly shown (e.g. Morozov *et al.* 2008) that such approaches lead to incorrectly recovered values. This is supported by the very large range of Q values or degree of frequency dependence published in the literature.

Nevertheless, potential biases in source properties introduced by insufficient or inadequate attenuation correction become especially important when analysing their magnitude dependence. While several authors reported evidence for a size dependence, or non-self-similar scaling of earthquakes (Archuleta *et al.* 1982; Gibowicz *et al.* 1991; Kanamori *et al.* 1993; Mayeda & Walter 1996; Jost *et al.* 1998; Prejean & Ellsworth 2001), many of these findings were later questioned as being possibly attributed to either recording bandwidth limitations (Ide & Beroza 2001), incomplete attenuation correction of surface data (Abercrombie 1995) or ignoring the possibility of frequency-dependent attenuation (Ide *et al.* 2003). Irrespective of potential bias and associated accuracy of earthquake scaling results, the scatter of observed stress drop variations is generally very large and spans several orders of magnitudes. Stress drop depends on the cube of the corner frequency, therefore, a small uncertainty in the determination of the corner frequency can result in a large stress drop uncertainty.

We focus our investigation onto source spectra of small earthquakes recorded in Switzerland. This represents an area with a low-to-intermediate seismicity rate that is covered by a dense high-quality digital seismometer network, which generally fulfills the coverage requirements for multipath separation methods that rely on redundant recordings. In the past, source studies of earthquakes in Switzerland and surrounding areas have been mainly limited to the calculation of magnitudes (e.g. Braunmiller *et al.* 2005; Edwards *et al.* 2010; Goertz-Allmann *et al.* 2011a) and, for the larger events, of moment tensor solutions (e.g. Kastrup *et al.* 2004; Deichmann & Ernst 2009). In this study, we systematically investigate spectral characteristics of the source for small to moderate earthquakes in Switzerland.

We employ two different spectral methods to isolate source spectra from path and site effects to study actual source processes. The two employed methods are closely related in the sense that they both exploit the redundancy contained in dense network recordings for the separation of source-, receiver- and path-dependent terms from the measured earthquake spectra. However, while one method separates between (relative) source, receiver and travel path terms in an entirely data-driven way, the other method requires specific model assumptions for the variation of attenuation and geometrical spreading in order to isolate their contribution from the source spectra. Systematic comparison of results from both methods and verification with synthetic tests reveal the impact of the attenuation model assumptions on the resulting stress drop estimates. The combined analysis of results from both methods helps in resolving trade-offs of the individual methods. Both methods produce similar results when assuming a frequency-dependent attenuation model. Despite the limited resolution in terms of overall residual misfit, we take this as evidence that the frequency dependence of Q is non-negligible in the investigated frequency range between 1 and 30 Hz.

Despite a reduction of scatter and quantification of uncertainties in stress drop estimates, we show that the remaining scatter prevents a quantitative investigation of the magnitude scaling behaviour of the analysed catalogue at a statistically significant level. The observed scatter of Brune stress drop is consistent with stochastic geomechanical models of induced seismicity assuming just a small random variation of the input differential stress (Goertz-Allmann & Wiemer 2013).

We first describe the background of extracting Brune stress drop from spectral fitting, and then describe the two spectral estimation methods with the associated data processing. We then discuss the results, their differences and the impact of different model assumptions. A synthetic test verifies (i) the necessity of assuming frequency-dependent attenuation in order to obtain consistent stress drop results between the two methods, and (ii) the capability of resolving lateral variations from a stress drop checkerboard test. A two-parametric fit of a power-law $Q(f)$ function to the separated traveltime terms reveals trade-offs in the inversion that prevent us from providing reliable quantitative estimates of the frequency dependence of Q. After discussing the inability to extract a reliable magnitude scaling relation from our results, we finally discuss the observed lateral variations in comparison to the main tectonic features of Switzerland.

2 DATA AND METHOD

Earthquakes used in this study are recorded at stations operated by the Swiss Seismological Service and some neighbouring stations from France, Italy, Austria and Germany between 1998 September and 2010 March within an epicentral distance of 300 km (Fig. 1). This catalogue contains about 5600 events between M_L 0 and M_L 5.4, of which about 1400 events between M_l 0.7 and M_l 5.3 remain for spectral analysis after application of several selection criteria. Stations of the Swiss Digital Seismograph Network (SDSNet) are equipped for the most part with Streckeisen STS-2 seismometers with sensitivity over periods from 120 to 0.02 s. Some stations are equipped with medium-period Lennartz LE-3D/5s seismometers, or broadband strong motion accelerometers (e.g. Kinemetrics Episensor). All traces are corrected for the instrument response and transformed to measurements of ground velocity, if applicable.

We apply two different spectral methods to estimate source parameters of earthquakes in Switzerland. Both methods analyse *S*-wave spectra and attempt to correct the spectra for path and site effects so that spectral variations can be attributed to source processes and near-source property variations. The first, data-driven method is a spectral stacking approach that exploits the redundancy of the captured wave paths for the separation of source, path and receiver effects (thereafter defined as Method 1). The second, model-dependent method (thereafter defined as Method 2) fits path attenuation, site effects and source components of each spectrum

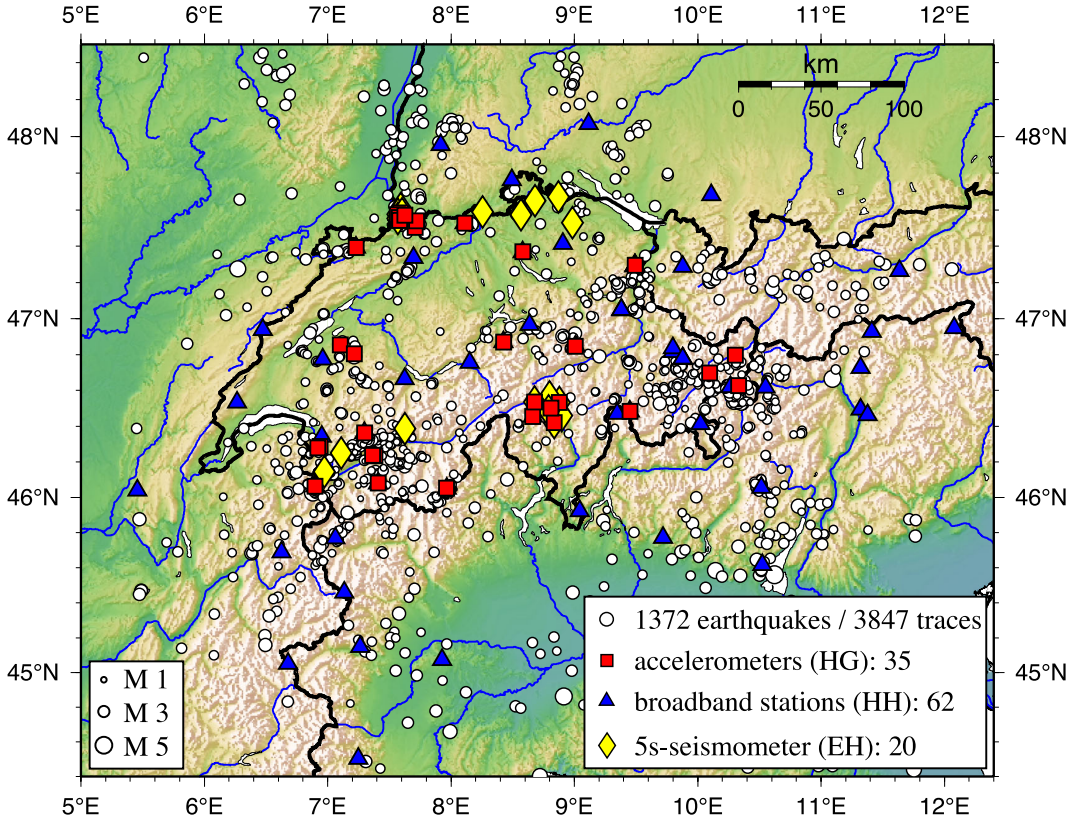

Figure 1. Location of earthquakes (circles), broadband seismometers (triangles), 5 s seismometers (diamonds) and accelerometers (squares) around Switzerland used in this study. The size of the circles scale with earthquake magnitude.

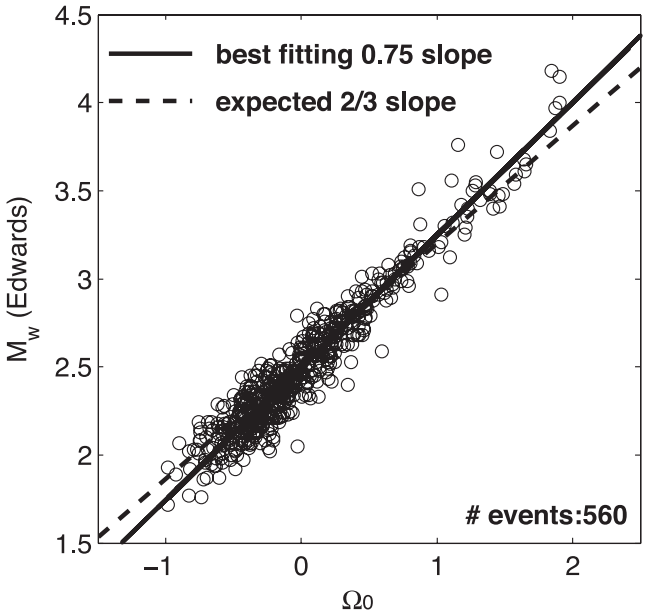

Figure 2. Moment magnitude M_w estimates from Edwards *et al.* (2010) of selected events versus relative moments. The dashed line shows a 2/3 relation and the solid line the best orthogonal fit with a slope of 0.75.

simultaneously while making specific model assumptions about the form of attenuation and geometrical spreading.

Common to both methods is the description (Model 2) or interpretation (Model 1) of the spectral shape of the velocity spectrum by means of the Brune (1970, 1971) ω^{-2} model,

$$u(f) = \frac{\Omega_0}{1 + (f/f_c)^2}\ , \tag{1}$$

where Ω_0 is the long-period amplitude and f_c the corner frequency. Assuming a circular fault, the stress drop $\Delta\sigma$ can then be determined, using the seismic moment M_0 and the source radius r, as (Eshelby 1957)

$$\Delta\sigma = \frac{7}{16}\left(\frac{M_0}{r^3}\right)\ . \tag{2}$$

The source dimension can be related to the corner frequency f_c as

$$f_c = \frac{k\beta}{r},\ \ \rightarrow\ \ \Delta\sigma = \frac{7}{16} M_0 \left(\frac{f_c}{k\beta}\right)^3\ . \tag{3}$$

The near-source shear wave velocity β is assumed to be variable with values taken from a local 3-D *P*-wave velocity model of Switzerland (Husen *et al.* 2003) and converted to *S*-wave velocity using a local v_p/v_s ratio of 1.73 (Diehl *et al.* 2005). In the following, we use $k = 0.37$ to estimate $\Delta\sigma$ from the *S*-wave spectrum. The value of $k = 0.37$ for the Brune model is considerably higher than the value of k for the Madariaga (1976, 1977) model ($k = 0.21$), and implies a stress drop 5.47 times lower for the Brune model than Madariaga's. The latter factor is important to keep in mind when attempting to compare results from this paper with other studies (e.g. Allmann & Shearer 2009).

While some of the data processing steps are different between the two methods, both methods analyse the same 1400 events. Processing differences between the two methods entail the definition of signal-to-noise selection criteria, and the windowing of data

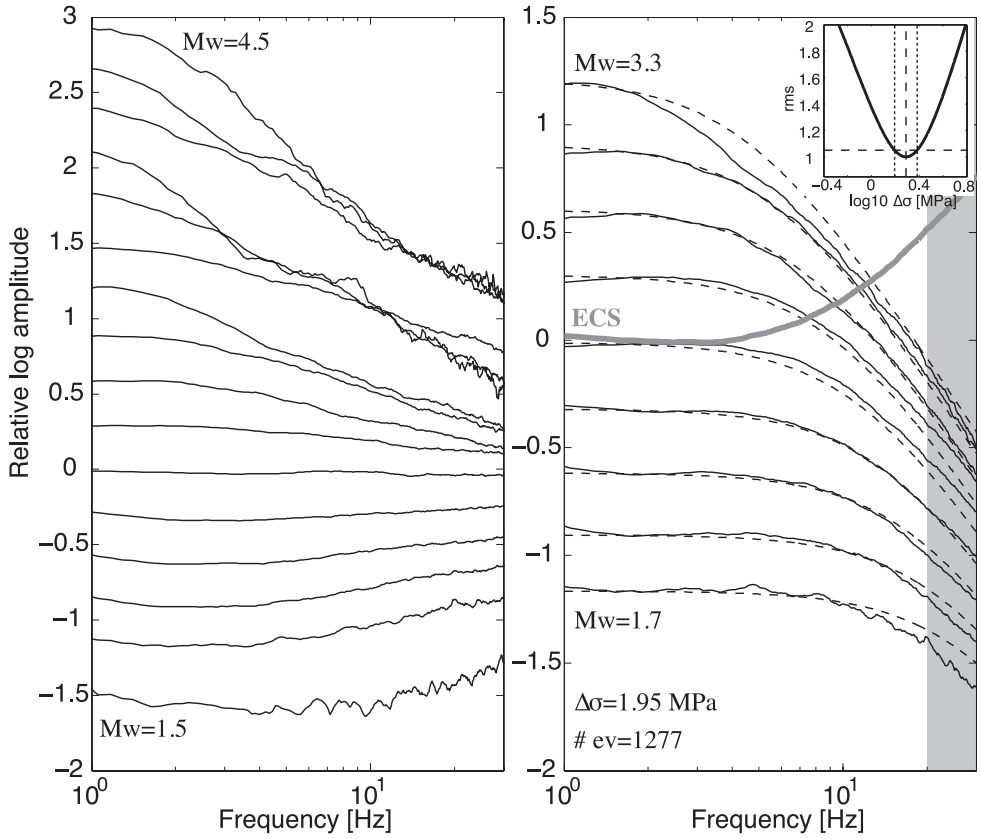

Figure 3. (a) Stacked relative source spectra in 0.2 moment magnitude M_w bins. (b) ECS-corrected source spectral stacks (solid black) compared to the best-fitting constant parameter source model with a stress drop of $\Delta\sigma = 1.95$ MPa for M_w bins between 1.7 and 3.3. The bold grey line shows the ECS. The grey-shaded area is outside the fitting range. Inset shows rms misfit versus log stress drop for estimating the best-fitting ECS. The vertical-dashed line marks the best-fitting stress drop (1.95 MPa) and the dotted lines the uncertainty estimates (1.56 and 2.42 MPa).

before spectral estimation, resulting in a slightly different effective bandwidth between the analysis methods. Both methods employ the same spectral fitting strategy based on a L2 norm applied on spectra resampled in the log domain. The main methodical difference is the assumption of the form of an attenuation and geometrical spreading model for the travel path correction of Method 2, while Method 1 removes any path effects by stacking without the need to make specific assumptions about the travel path term. The advantage of Method 1 comes at the expense of obtaining only relative source term variations that need to be converted to absolute spectral shapes by means of an empirical correction. In the following, we separately describe the differences between individual processing steps of the two methods.

2.1 Method 1: Spectral stacking method

Since Method 1 relies on the analysis of fixed-length time windows resulting in equal sampling in the frequency domain, all traces with a different sampling rate are first resampled to 120 Hz after applying an anti-aliasing filter. Then, each time-series is windowed over 1024 sample points starting 0.2 s before the S-wave pick. Manual picks are preferred if available otherwise automatic picks are used (Diehl *et al.* 2009). If no S-wave pick is available, we compute the pick from the *P*-wave pick using a constant 1.73 v_p/v_s scaling factor. Velocity spectra are computed using the multitaper spectral estimation library of Prieto *et al.* (2009). We require a minimum signal-to-noise ratio (SNR) of at least 3 in each frequency bin between 1 and 20 Hz. The SNR is estimated using a moving window average over two neighbouring frequency sample points. The noise window is selected before the *P* wave arrival. We also require each event to be recorded by at least six different traces including both, N and E components, in order to average out directivity effects between different azimuths.

In the log domain, the velocity spectrum can be described by a linear combination of the source, the attenuation along the travel path and site effects at the receiver, including the instrument response. To study the earthquake source we can separate the source term from other terms by means of an iterative least-squares stacking approach where we exploit the redundancy contained in the data. The traveltime term is discretized in 1 s bins. For further details about the spectral stacking approach, the reader is referred to Shearer *et al.* (2006) and Allmann & Shearer (2007). Note that with this method we isolate relative variations of the source spectra between all events and we have to apply an empirical correction with the assumption of a specific source model afterwards to obtain absolute source spectra.

The seismic moment M_0 is proportional to the long-period spectral amplitude Ω_0 of the source spectrum. We estimate the relative seismic moment from the average spectral amplitude between 1.2 and 1.6 Hz of each relative source spectrum. We cannot estimate Ω_0 at lower frequencies since the SNR deteriorates rapidly below about 1 Hz, especially for the smaller magnitude events. The calibration to absolute M_w can be performed with a small percentage of the data set for which indepentently obtained absolute M_w estimates are available. We use M_w obtained by Edwards *et al.* (2010) to calibrate

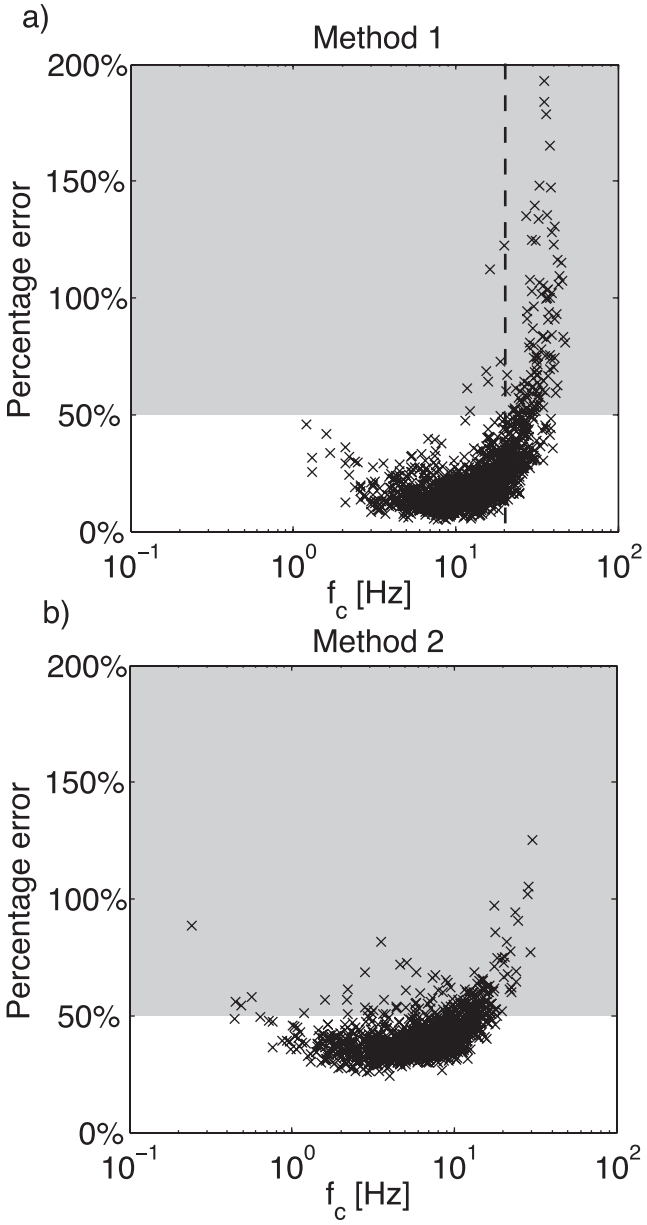

Figure 4. Percentage error of corner frequencies for (a) Method 1, and (b) Method 2. The dashed vertical line in (a) marks the upper fitting limit.

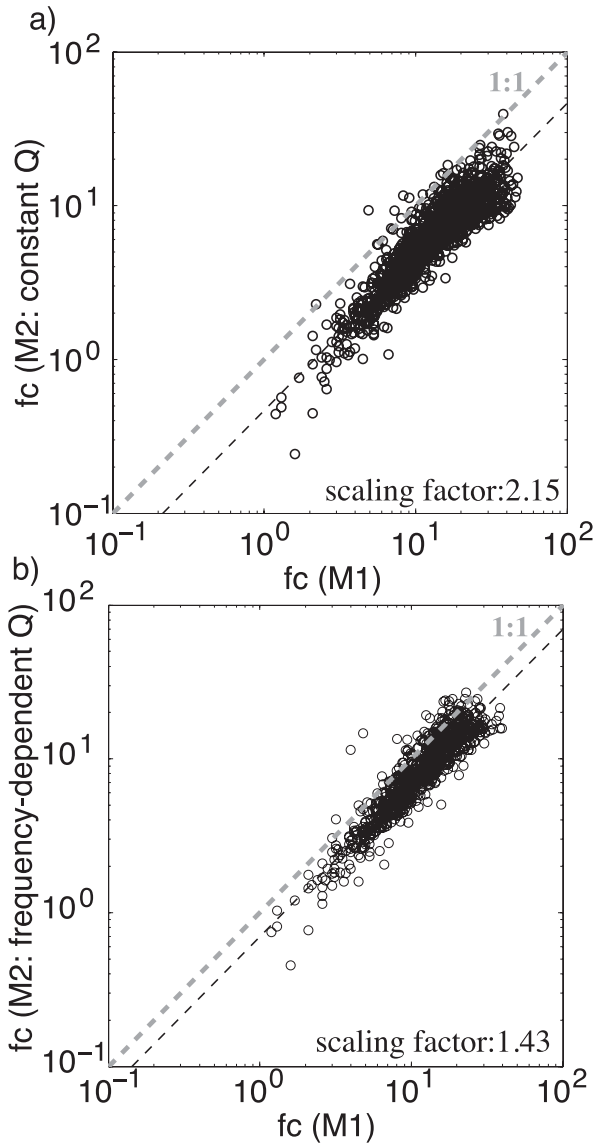

Figure 5. Comparison of corner frequencies between Method 1 and Method 2 if (a) a frequency-independent attenuation model is used in Method 2 and (b) a frequency-dependent attenuation model is used in Method 2. The grey-dashed line shows a 1:1 relation.

our relative M_w estimates (proportional to $2/3\,\Omega_0$) to absolute M_w (Fig. 2). The rms difference of 2.5 between the two is used as a constant shift to scale the relative M_w to absolute values. Note that we observe a slight deviation from an expected 2/3 slope between Ω_0 and absolute M_w in Fig. 2. However, this observed difference does not bias the obtained stress drop estimates.

We label Method 1 'data-driven' specifically in respect to its ability of separating relative source, travel path and site terms without a specific model assumption. However, it still relies on a ω^{-2} source model assumption to obtain interpretable absolute source terms. The assumption of a ω^{-2} model for interpretation of the derived source spectra is a feature it shares with Method 2. In order to correct the relative source spectra to absolute spectral shapes, we use an empirical correction spectrum (ECS). First, all isolated source spectra are stacked into 0.2 units of M_w. Secondly, we simultaneously fit an ω^{-2} model (Brune 1970) with constant stress drop across magnitudes to the spectral stacks. We only use magnitude bins with a sufficient number of events in them for the fitting, in this case $M_w = 1.7$–3.3 (see Fig. 3). The average difference between the best-fitting model and the observed spectral stacks at each frequency sample results in the ECS (bold grey line in Fig. 3b). The ω^{-2} gives a good overall fit to our data: a grid-search test with a variable fall-off rate ω^{-n} revealed that $n = 2$ gives overall the smallest misfit to the data.

The best-fitting ECS stress drop for our set of parameters is 1.95 MPa (Fig. 3b) with a variance between 1.56 and 2.42 MPa (inset Fig. 3b). We estimate the uncertainty of the ECS stress drop from the rms misfit function following the approach of Viegas *et al.* (2010). First, we normalize the rms misfit function by the obtained minimum, and secondly, we determine the stress drop limits from a 5 per cent increase of the rms. The ECS is used in a subsequent step to correct the individual relative source spectra to absolute spectral shapes. The absolute value of the ECS stress drop determines the mean stress drop of all individual events. Therefore, any variability of the ECS stress drop has a direct effect on the absolute stress

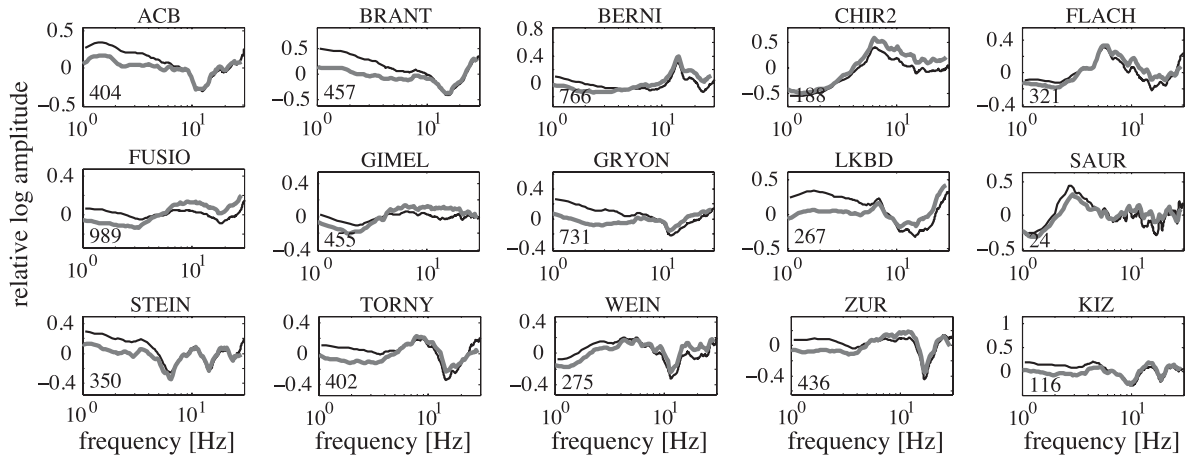

Figure 6. Example normalized receiver spectra of selected stations corrected for κ obtained using Method 1 (thin black) compared to site effect estimates using Method 2 (bold grey). The number of traces stacked per station (Method 1) is marked. Note the good match between the two studies.

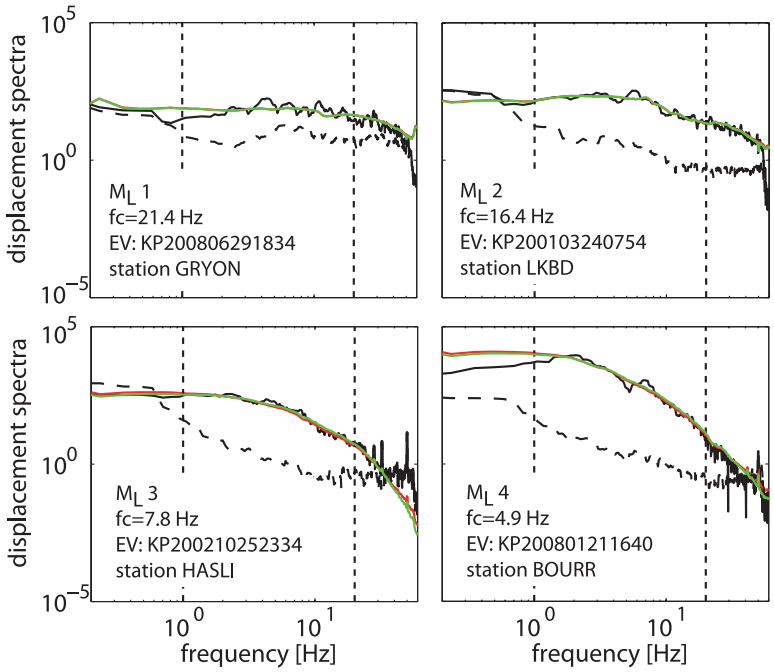

Figure 7. Four example signal (black solid) and noise (black-dashed) displacement spectra for magnitude $M_L = 1$–4. The red line shows the theoretical fit (source model + attenuation model + receiver model) to the displacement spectra using a frequency-dependent attenuation model and the green line shows the fit using a constant Q model. The vertical-dashed lines mark the fitting boundaries of 1–20 Hz for Method 1.

drops determined with this method. To investigate the variability and uncertainty of the ECS stress drop due to the event selection, we apply a bootstrap resampling method. We create 100 resamples of the original data distribution (N events) by randomly choosing N events with repetition. From each resample we can estimate an ECS stress drop. The median ECS stress drop is 2.51 $\pm$ 1.26 MPa. This mean ECS stress drop is also robust with respect to other processing parameters. If we apply the bootstrap method to 0.3 N events of the original data distribution, the median ECS stress drop is 2.57 $\pm$ 3.8 MPa. This shows that the mean ECS stress drop does not depend strongly on the overall number of events used for the processing. However, the standard deviation of the mean ECS stress drop increases significantly by reducing the number of events. Therefore, the method may not be stable if too few events are available or if the data are too limited by selection criteria. Note that the bootstrapping only shows the uncertainty of the ECS stress drop that is introduced by random event selection. Other processing parameters, such as the magnitude fitting range can also have an effect on the ECS stress drop. For the Swiss data, the ECS stress drop becomes very unstable if the larger magnitude bins ($M_w \geq 3.3$) are included in the processing. This can be explained by a smaller number of events in these magnitude bins. The ECS stress drop is, therefore, only computed for magnitude bins between M_w 1.7 and 3.3.

After correcting each source spectrum with the computed ECS, we can estimate corner frequencies f_c and stress drops of individual events using eqs (1) and (3). The best-fitting f_c is found by a least-squares fit between the corrected source spectra and the theoretical model after resampling the data regularly in the log domain. Note that relative spectral variations between individual events do not

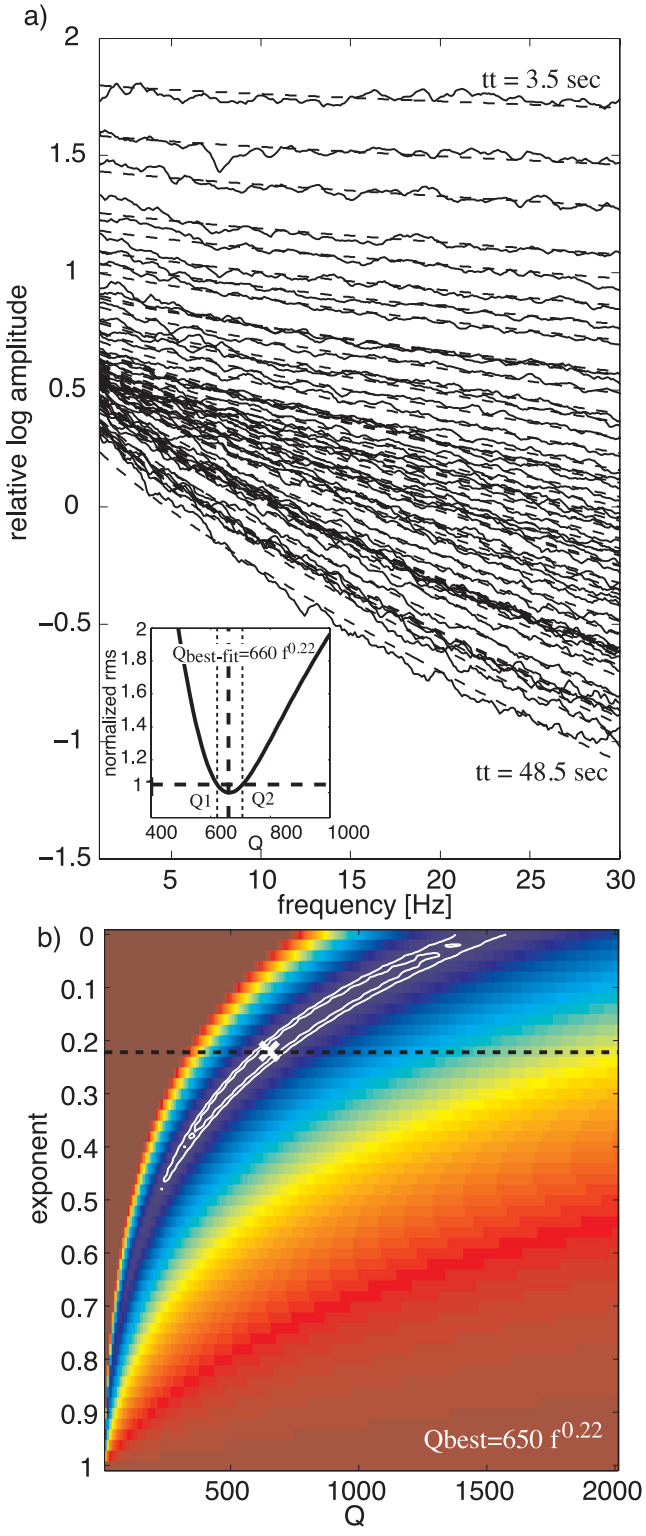

Figure 8. Two-parametric fit of a frequency-dependent Q to the isolated traveltime terms of Method 1. Traveltime terms in (a) are binned in 1 s intervals from 3.5 to 48.5 s. We clearly observe a deviation from a linear decay pointing to a frequency dependence. (b) Normalized misfit function of two-parametric grid search. The best-fitting attenuation function is indicated by the white cross together with the 5 and 10 per cent error contours. Inset in (a) shows a section along the dashed line in (b). Misfit minima (area within the 10 per cent error contour) describe a trade-off between Q_0 and the fall-off rate.

depend on the ECS calibration. Again we estimate the uncertainty of each corner frequency estimate (Δf_c) from the rms misfit function following the approach of Viegas *et al.* (2010). In some cases, the rms misfit function does not have a well-defined minimum leaving the corner frequency unconstrained at one or both limits. For these cases, we set the corner frequency limits to the fitting limits of 0.1 and/or 100 Hz. The percentage error ($\Delta f_c/f_c$) of the corner frequency is shown in Fig. 4(a). Most events have an error smaller than 50 per cent. The errors rapidly increase for f_c estimates outside the upper fitting range (20 Hz).

2.2 Method 2: Simultaneous fitting method

Data processing for the simultaneous fitting method follows Edwards *et al.* (2008) and Edwards & Rietbrock (2009). In brief, the multitaper fast Fourier transform algorithms of Park *et al.* (1987) and Lees & Park (1995) are applied to an analysis window whose position and duration is based on the *S*-wave arrival and the arias intensity of the recorded time-series. The aim is to encapsulate the main duration of shaking defined by 5–95 per cent of the energy from the earthquake. The resulting frequency spectra have differing minimum, maximum and delta frequency, depending on the length of the time window used. However, the minimum frequency available to the subsequent inversion is typically between 0.1 and 1 Hz, with the maximum ranging from 10 to 30 Hz. Noise estimates are taken from the recording before the *P* phase arrival and are carefully compared with the signal in the frequency domain in order to retain only the highest quality data: a SNR of at least 3 over a bandwidth of at least one order of magnitude in length is required to retain the data. As with Method 1, for very close recordings the noise due to the *P* coda may not be fully accounted for. However, in order to minimize the risk of underestimating the noise level, we adopt the conservative approach of Edwards *et al.* (2010): increasing the noise spectrum until intersection with the signal spectrum at the highest (e.g. 50 Hz) and lowest (e.g. 0.01 Hz) frequencies of the spectrum, before measuring the SNR. All data are converted to velocity spectra if applicable and the instrument response is removed.

Following the selection and processing of data, the absolute values of M_w for events with more than five recordings are extracted using a two-stage regression that deconvolves the source, path and site effects as detailed in Edwards *et al.* (2008). The earthquake source is based on the Brune (1970, 1971) model, with geometrical attenuation described by a model with segmented exponential decay taken from Edwards *et al.* (2011), which accounts for post-critical reflections from the Moho and major phase transitions. In Edwards *et al.* (2010), it was shown that the M_w computed using the spectral fitting method are consistent with the M_w computed using a moment tensor solution based on broad-band waveform fitting of local Swiss earthquakes of $M_w = 2.8$–5.0, with a negligible offset and standard deviation of less than 0.1.

M_w computed using Method 2 depends on a good azimuthal coverage of recordings. This is quantified by including only events where the circular standard deviation of azimuths is greater than 30°. For smaller events, the relatively large interstation spacing results in few recordings passing the quality control procedure. Consequently, there also exists a minimum magnitude for which the method is stable. This is highly dependent on the location of the earthquake and the level of background noise. However, solutions for earthquakes with $M_L < 1.0$ are rarely available after quality control and signal processing procedures.

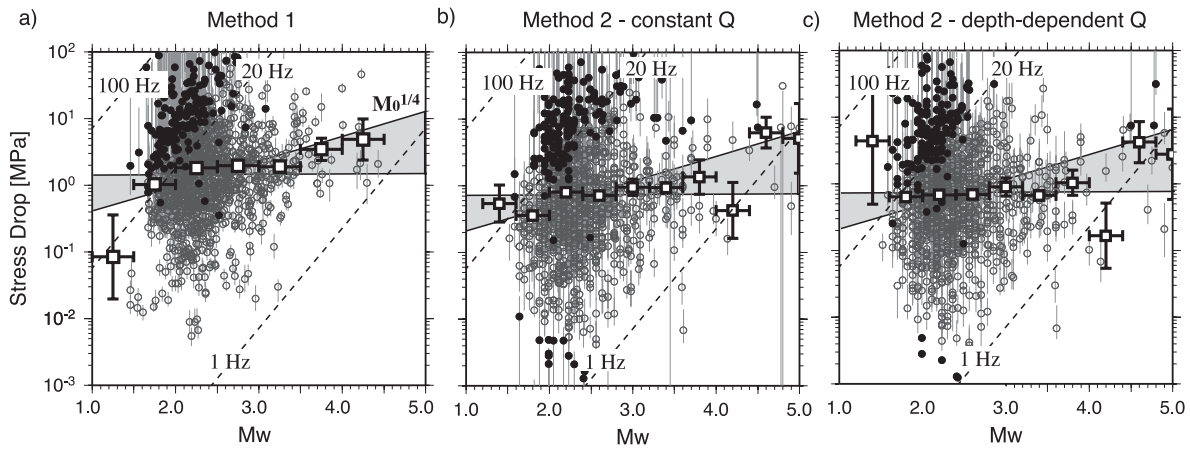

Figure 9. Stress drop versus moment magnitude M_w for (a) Method 1 (black circles mark events with a percentage error higher than 50 per cent and are excluded in further analysis), (b) Method 2 using a constant Q model and (c) Method 2 using a depth-dependent Q model and corrected for depth-dependent shear wave velocity. Grey vertical bars indicate the uncertainty of stress drop estimates. The median stress drop and standard error are shown by the squares. The dashed lines show constant corner frequency for 1, 20 and 100 Hz. The grey-shaded areas show possible ranges for magnitude scaling between M^0 and $M^{1/4}$.

Several possibilities exist to consider attenuation in the simultaneous fitting method. The quality factor Q can be a laterally and vertically constant frequency-independent bulk factor, a depth-dependent factor or a frequency-dependent function with two parameters, the intercept Q and the slope of a power-law decay with frequency.

Near-receiver terms can contain contributions from site effects at the stations and near-receiver attenuation effects. The near-receiver attenuation can be described by an independent attenuation parameter κ (e.g. Anderson & Hough 1984). In fact, κ simply defines the t^* parameter in the near-surface as

$$\kappa = \frac{R_S}{Q_S \beta_S}, \tag{4}$$

where R_S indicates the path distance, Q_S the attenuation and β_S the shear wave velocity in the near surface. κ can be estimated from the slope of a straight line in a log-linear plot of spectral amplitude A corrected for crustal attenuation effects versus frequency f since $A(\omega) \propto e^{-\omega\kappa/2}$ and, therefore, $\log_{10}(A) \propto -1.364 f\kappa$ with $\omega = 2\pi f$. Method 2 simultaneously fits for near-receiver κ as well as Q along the travel path, representing the attenuation away from the near surface. The corner frequency error estimates are overall higher for Method 2 except for at the boundary of the frequency bandwidth (Fig. 4).

We show in the following the impact of these different attenuation models on the resulting stress drop values, and the model requirements that are needed to match inverted stress drop results from this method with results obtained by the data-driven Method 1.

3 DIFFERENCES BETWEEN BOTH METHODS AND CONSTRAINTS ON ATTENUATION MODEL

Since both methods use the same data, they should ultimately lead to similar results if the underlying assumptions were consistent with the data. The fact that they do not is an indication that either the underlying physical assumptions need to be adapted or one or both methods are subject to unresolvable trade-offs. If trade-offs are resolved differently by a data-driven versus a more model-constrained method, we can exploit this behaviour to constrain some of the potentially ambiguous parameters. Finding the root cause for the apparent differences between the results from both methods is described in the following.

The first observation is that both methods lead to robustly consistent results regarding a number of aspects (e.g. relative lateral variations, relative separation of site terms), except one thing: depending on the assumptions for the attenuation model in Method 2, the mean of the absolute corner frequency values is significantly different between both methods. This is illustrated in Fig. 5, which shows a cross-plot of inverted corner frequency values between both methods. If we assume a frequency-independent Q in Method 2, the inverted corner frequencies are different by a mean factor of more than two (Fig. 5a). Note that due to the cubic dependence between corner frequency and stress drop (see eq. 3), this corner frequency difference would translate into a stress drop difference of almost one order of magnitude. This mean difference does not change significantly if we assume a depth-dependent Q or any other variation of the attenuation dependency short of a frequency dependence. Likewise, the observed bulk difference cannot be explained by the differences in processing described above. That the underlying attenuation model manifests itself as a bulk shift, and not in, say, a different magnitude scaling of stress drop is at first rather puzzling. In particular, since we know that the price for model independence of Method 1 is the fact that we can only obtain relative, not absolute, source, path and receiver terms. Therefore, before focusing on the attenuation model assumptions, we conducted extensive testing to rule out any processing effects, covering the following aspects:

(1) Changing the parameters for the ECS correction applied in Method 1 influences the absolute values somewhat, but cannot account for the observed factor of two differences between the two methods. Forcing the ECS stress drop of Method 1 to the median stress drop of Method 2 results in overall larger misfits, and unstable results.

(2) Differences in the signal-to-noise selection strategy results in minor differences between the catalogue analysed by both methods. These differences do not exceed 5 per cent of the overall number of events and are easily captured by the uncertainty estimates

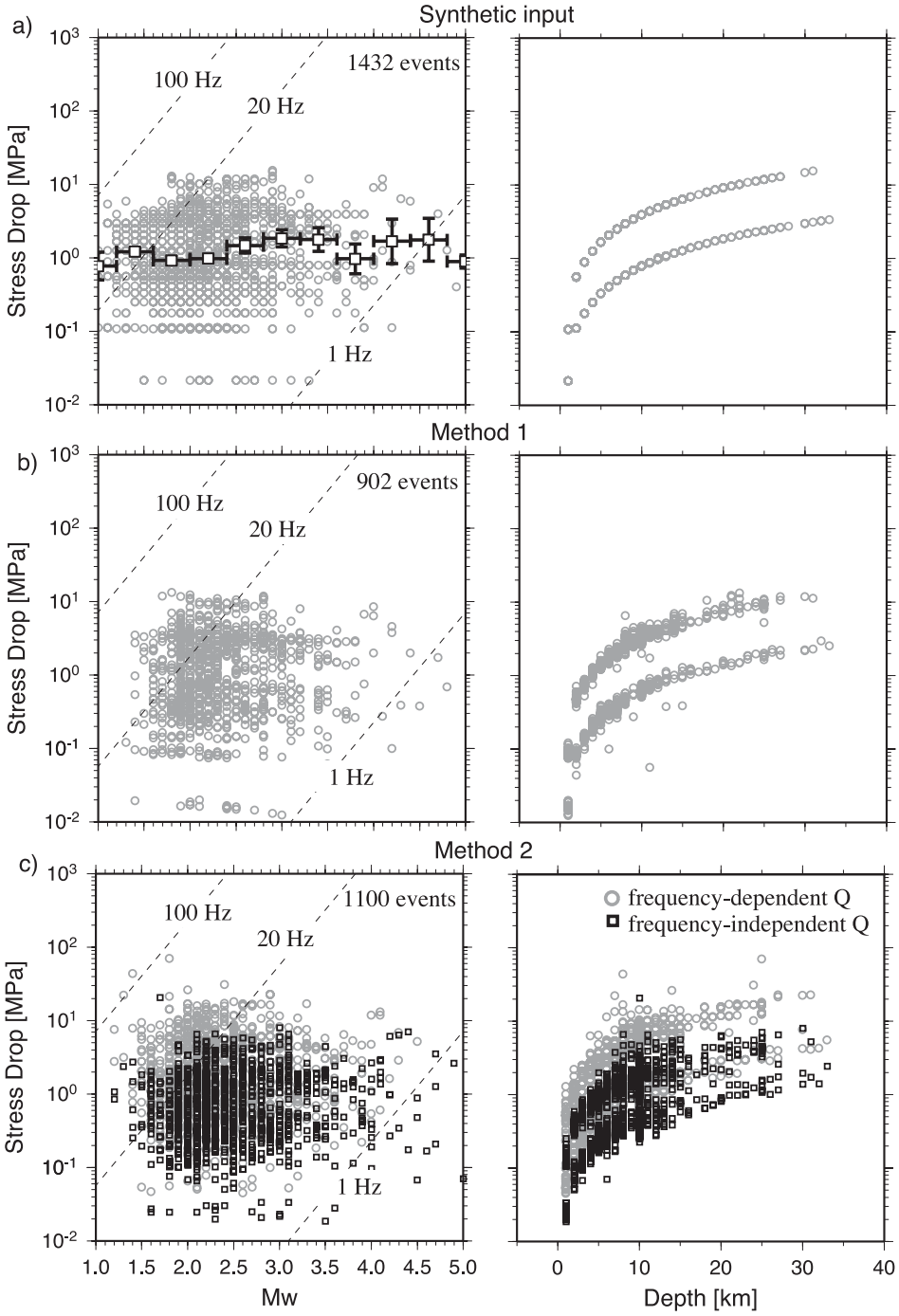

Figure 10. Stress drop versus moment magnitude M_w (left columns) and stress drop versus event depth (right columns) for (a) synthetic input data, (b) inverted data of synthetics using Method 1 (median stress drop and standard error are shown by the squares with error bars) and (c) inverted data of synthetics using Method 2 for a frequency-dependent Q inversion (grey circles) and a frequency-independent Q inversion (black squares). The dashed lines show constant corner frequency for 1, 20 and 100 Hz.

from bootstrap resampling, and, therefore, cannot account for the observed bulk shift.

(3) Different windowing strategies (fixed window length in Method 1, variable window length in Method 2) result in a different effective bandwidth between the two methods. The effective bandwidth has an influence on the estimated errors, as is shown in Fig. 4. Errors strongly increase towards the perimeter of the frequency band considered in the signal-to-noise estimation. Leaving out all data points that exceed 50 per cent error do not change the result significantly and cannot account for the observed bulk shift in corner frequency values.

(4) Investigation of near-receiver terms reveals a remarkably consistent and stable result between both methods. While not directly considering κ, Method 1 can estimate κ by detrending the station terms and fitting κ according to eq. (4). Fig. 6 compares detrended station terms of Method 1 with station terms of Method 2 for some example stations. Detrended spectra from Method 1 have also been shifted vertically as they are determined in a

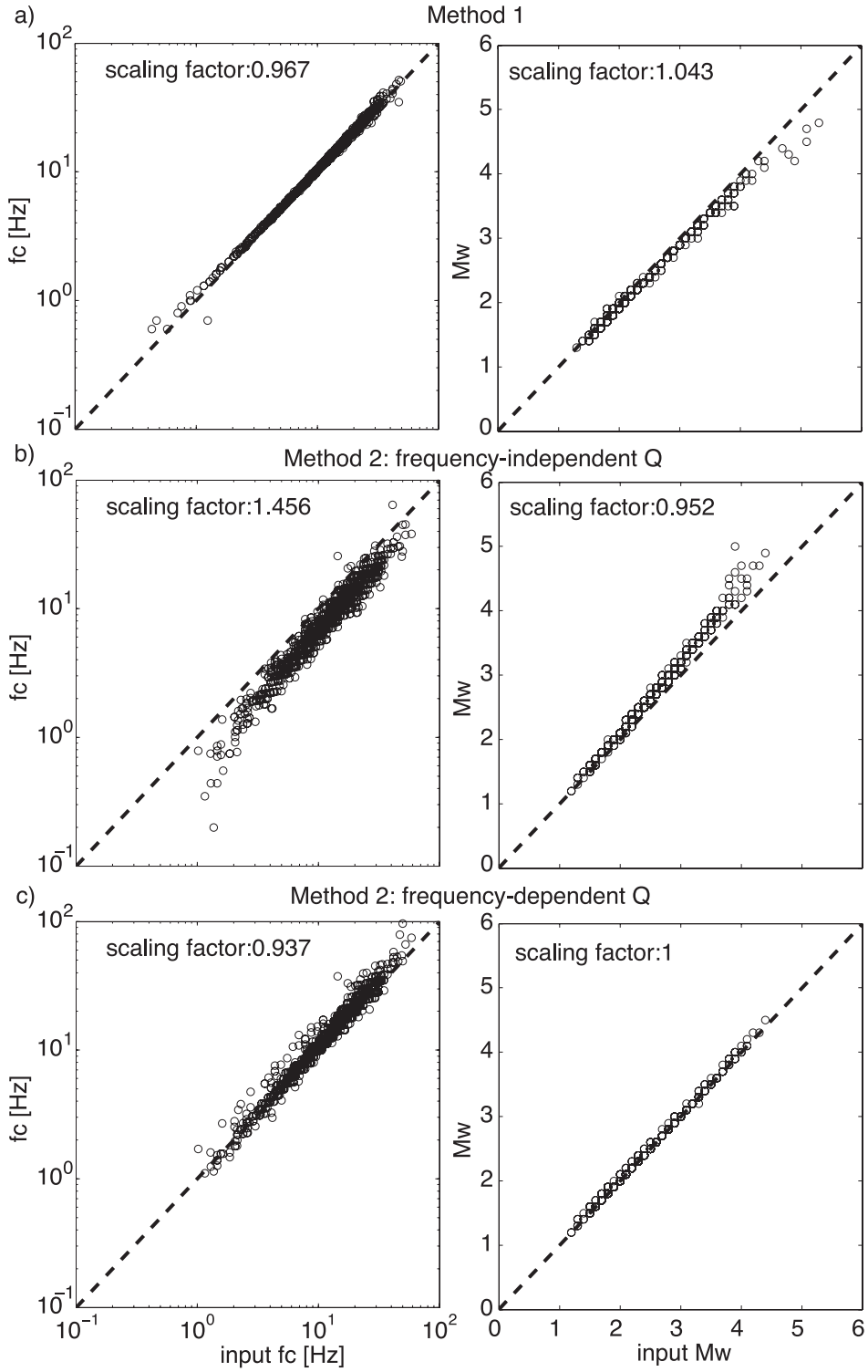

Figure 11. Inverted output corner frequency of synthetic data versus synthetic input corner frequency (left columns) and inverted magnitude of synthetic data versus synthetic input magnitude (right columns) for (a) using Method 1, (b) using Method 2 with a frequency-independent Q model and (c) using Method 2 with a frequency-dependent Q model. The dashed lines show a 1:1 relation. The mean scaling factor is indicated.

relative sense up to an arbitrary constant. Despite high scatter (expected due to strong trade-offs with site effects), the κ values obtained through both methods are consistent with each other and again cannot account for the observed bulk shift in stress drop.

After ruling out the above possibilities as cause for the different average stress drops, we continued by investigating the underlying physical model assumptions. Using a parametric inversion, such as Method 2, allows us to test specific model assumptions for their ability to lead to results that are consistent between both methods.

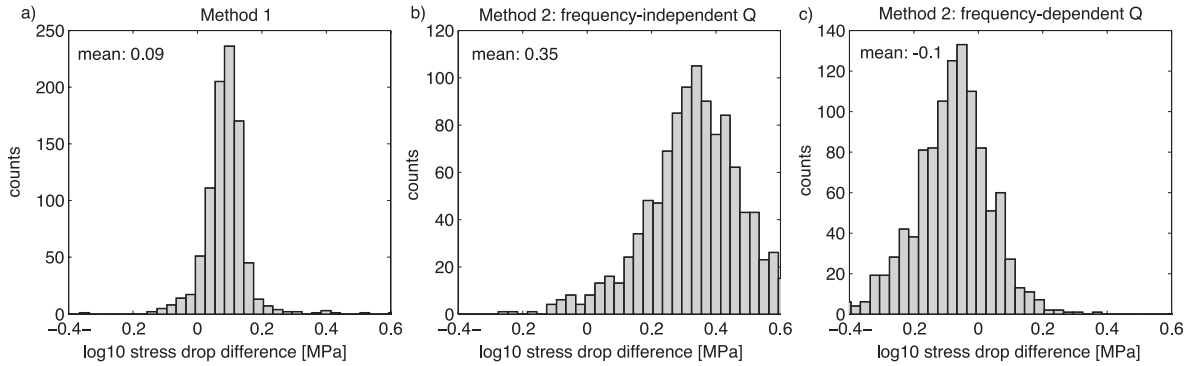

Figure 12. Histogram of log stress drop difference between synthetic input and inverted output of synthetic data using (a) Method 1, (b) Method 2 with a frequency-independent Q model and (c) Method 2 with a frequency-dependent Q model. The mean value is indicated.

We tested several different attenuation models, including average, depth-dependent and frequency-dependent Q. In the end, only the assumption of a power-law frequency-dependent whole-path attenuation is able to significantly reduce the mean shift between results of both methods (Fig. 5b). Based on the results of Edwards *et al.* (2011), Method 2 assumes a fixed power-law dependence of

$$Q(f) = Q_0 f^{0.3} \,, \tag{5}$$

where the intercept factor Q_0 is determined from the data, resulting in a value of 467. Fig. 7 shows four example spectra between M_l 1 and 4, together with the respective noise spectra estimated before the P-wave arrival. The source model fit for constant or frequency-dependent attenuation is shown by the green and red lines, respectively. Source, receiver and path terms modelled from the inverted parameters have been stacked for comparison with single-station spectra. It is difficult to distinguish between the different attenuation models in this domain, which underscores that only the combination of both methods can resolve some of the spectral trade-offs. Assuming a higher fall-off rate would further reduce the difference in corner frequencies between the methods. However, as corner frequencies, site-term kappa and moment magnitudes are all fitted simultaneously, one has to be careful not to overparametrize the inversion. Therefore, no inversion for the attenuation fall-off rate was attempted.

Since no *a priori* assumptions need to be made for the separation of propagation path terms by spectral stacking (Method 1), we can use it basically as a benchmark. We test to what extent a frequency-dependent Q is consistent with the isolated traveltime terms of Method 1. For this purpose, we apply a two-parametric grid search over Q_0 and the exponential decay of the frequency (see eq. 5) to the traveltime terms of Method 1 between 1 and 30 Hz (Fig. 8). The reader is referred to Shearer *et al.* (2006) for a description of the process that yields propagation path terms for each traveltime bin. We note a deviation of the traveltime terms in Fig. 8(a) from a straight line, providing evidence for a frequency-dependent Q. It should be noted that the traveltime terms have been extracted completely model independent. No source model assumption can, therefore, influence them or the resulting attenuation model. The best-fitting attenuation function shown in Fig. 8(b) is consistent with the frequency-dependent model assumption of Method 2, which results in a better fit between the two methods (Fig. 5b). However, the misfit function from the two-parametric grid search (Fig. 8b) also reveals a trade-off between the intercept Q_0 and the fall-off rate that is not clearly resolvable. Tests with varying frequency bandwidths revealed that the trade-off is the stronger, the narrower the bandwidth over which the traveltime terms are evaluated. The decrease of the SNR below 1 Hz and above 30 Hz prevents us from opening up the bandwidth further with this data. It has to be noted that the traveltime terms of Method 1 are not fully incompatible with a higher, frequency-independent constant Q, which would lead to similar misfits. We base this statement on the observation that the misfits for a constant Q would be still within the region of 10 per cent deviation from the global minimum (following Viegas *et al.* 2010, see white contours in Fig. 8b). However, in combination with the observation that matching corner frequencies between the two method can only be achieved if Q is assumed to be frequency dependent, we conclude that the data suggest a frequency dependence of Q between 1 and 30 Hz in Switzerland.

4 MAGNITUDE SCALING AND SELF-SIMILARITY

When investigating earthquake stress drop over a wide range of magnitudes, self-similarity of earthquake scaling is always a corollary question. Self-similar earthquake scaling implies that stress drop observations are independent of magnitude. While a range of observations over the last decades imply that this may be the case (Abercrombie 1995; Allmann & Shearer 2009, and references therein), there are other observations, (e.g. Mayeda & Walter 1996) that suggest that a $M^{1/4}$ or similar scaling might also be possible. Indeed, Edwards & Fäh (2013) found that in order to match macroseismic intensities observed for historical Swiss events with $M > 4.5$, a stress drop of 6–8 MPa was required, which is higher than the values obtained in this study for smaller events. Often the large scatter of stress drop observations coupled with the finite frequency bandwidth of available data does not allow to distinguish between these two models in a reliable manner over a wide enough magnitude range. Since both methods used in our study use different window lengths (fixed for Method 1 versus variable for Method 2), we can at least investigate a possible influence of the effective frequency bandwidth on the magnitude scaling. In particular, if the method with the narrower effective bandwidth (in this case Method 1 using a fixed window length) would show hints of magnitude scaling compared to the wider bandwidth Method 2, it could be an indication that the investigation bandwidth causes a bias in the magnitude scaling. As a matter of fact, this behaviour is not observed. For both methods, we can not statistically justify a dependence of stress drop with magnitude over the analysed range ($1.5 < M_w < 5$, Fig. 9) amidst the large scatter. However, a trend of increasing stress drop would coincide with the results of

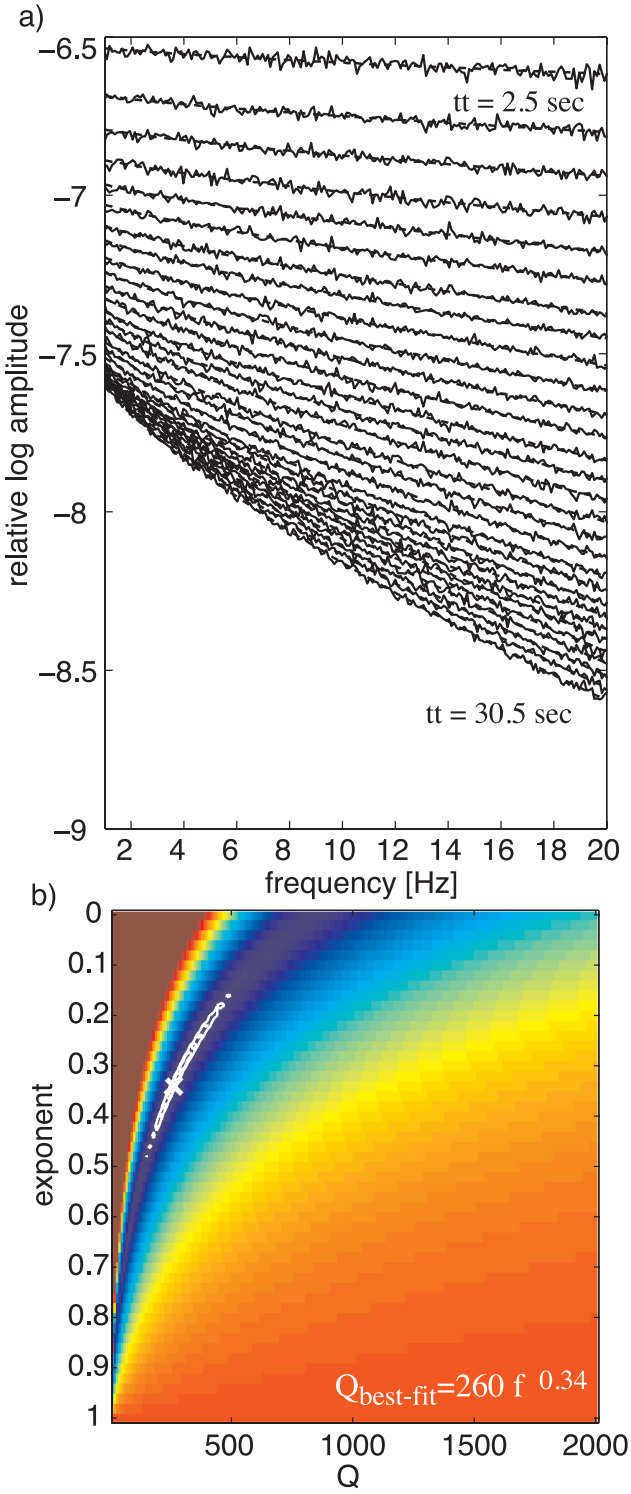

Figure 13. Two-parametric fit of a frequency-dependent Q to the isolated traveltime terms of the synthetic data using Method 1. Traveltime terms in (a) are binned in 1 s intervals from 2.5 to 30.5 s. (b) Normalized misfit function of two-parametric grid search. The best-fitting attenuation function is indicated by the white cross together with the 5 and 10 per cent error contours.

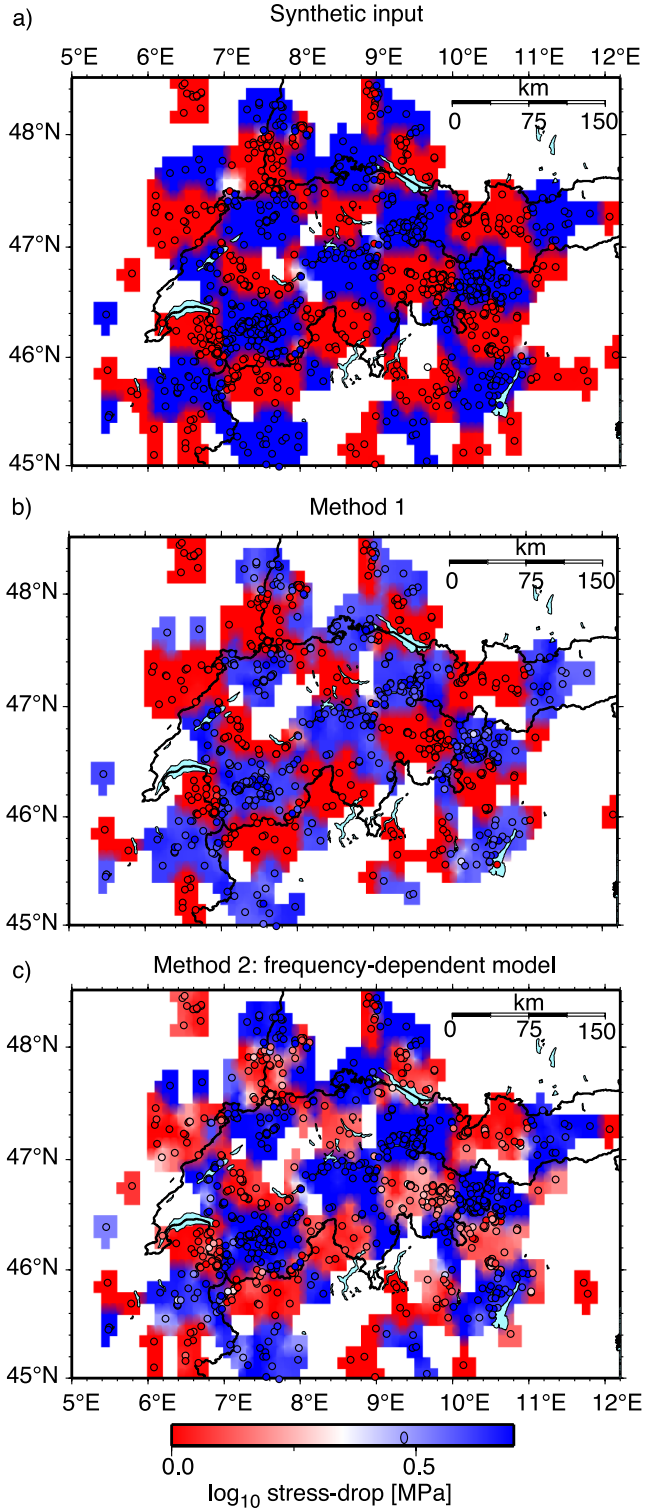

Figure 14. Depth-corrected lateral stress drop variations for (a) synthetic input data, (b) inverted data of synthetics using Method 1 and (c) inverted data of synthetics using a frequency-dependent model in Method 2. Colour denotes log stress drop interpolated in between individual events. Stress drop in checkerboard fashion is well recovered by the inversion.

Edwards & Fäh (2013) for high-magnitude Swiss earthquakes. We have indicated the effective frequency bandwidth for both methods by the dashed lines in Fig. 9. Method 1 is fitting corner frequencies between 1 and 20 Hz, corresponding to the frequency range over which the SNR selection criterion is applied. The variable window lengths of Method 2 yield an effective bandwidth of 0.1 to 30 Hz. Note that we are able to resolve corner frequencies beyond the fitting range. However, the uncertainties of the least-squares fit increase

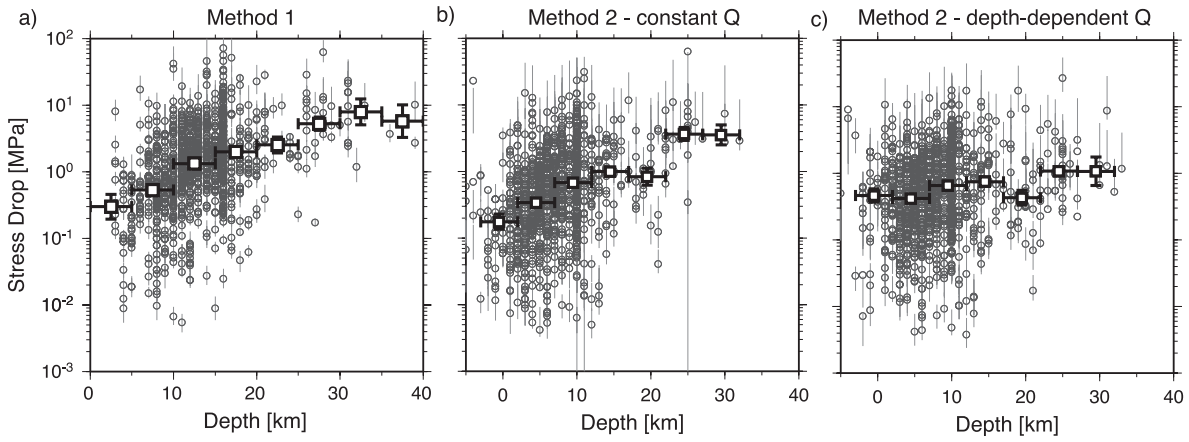

Figure 15. Stress drop versus focal depth for (a) Method 1, (b) Method 2 using a constant Q model and (c) Method 2 using a depth-dependent Q model and corrected for depth-dependent shear wave velocity. Grey vertical bars indicate the uncertainty of stress drop estimates. The median stress drop and standard error from bootstrap resampling are shown by the squares. Note that all focal depth have been shifted by 3 km to avoid negative depth values for processing purposes.

and most events have a percentage error in f_c larger than 50 per cent (Fig. 4). For Method 1, we have indicated all stress drop results with a corner frequency error above 50 per cent in black. While these dots should not be visually interpreted, we have to keep the corresponding values for a regression of possible scaling. Shaded areas in Fig. 9 show possible ranges for magnitude scaling between M^0 (no scaling) and $M^{1/4}$ (Mayeda & Walter 1996).

It should be noted that the application of a SNR selection criterion as is used by both methods preferentially excludes events at particularly low stress drops as the bulk of the energy for such events would fall into the high-noise ocean microseism band below 1 Hz. Likewise, anthropogenic noise increases upwards of 10 Hz, therefore, low-magnitude events with high stress drops (upper left quadrant of Fig. 9) may be overproportionally excluded from the selection. Therefore, the SNR selection criterion may in effect introduce a bias suggesting a magnitude scaling of stress drops.

While we cannot exclude the possibility of a magnitude stress drop scaling relation, such as proposed by Mayeda & Walter (1996), we find that we cannot pinpoint one or the other with any statistical significance. Our data do not provide sufficient evidence and the possible causes of bias are too large.

5 SYNTHETIC TEST

We create synthetic data in the frequency domain to test the two different methods of deconvolution. This test serves to verify our conclusion that the bulk difference in inverted corner frequencies between the two methods is a manifestation of unconsidered frequency dependence of attenuation in the study region. We carefully construct a synthetic data set that includes a depth-dependent shear wave velocity and frequency-dependent Q structure. It also allows for the influence of post-critical reflections from the Moho and the transition from spherical to cylindrical spreading regime in addition to site-specific amplification and attenuation effects.

Furthermore, a built-in checkerboard test will reveal to what extent and under what circumstances both methods are able to resolve lateral source parameter variations that may be interpretable in a tectonic context. We use the same source–receiver configuration found in the real data for our synthetic test in order to mimic a possible footprint of the geometry. For the synthetic catalogue we make a purely arbitrary assumption that $M_\mathrm{L} = M_\mathrm{w}$, as M_L is the magnitude that is directly measured and available for all earthquakes in the Swiss catalogue and we want to closely imitate the statistical distribution present in the real data set. One of the factors limiting the deconvolution of spectral data is the noise present on the recording. In order to correctly account for this limitation, noise is added to the spectra by adding the original noise recorded on the sensor immediately prior the specific event. The noise at low and high frequencies are altered to intersect the model spectra at very low (e.g. 0.05 Hz) and high frequencies (e.g. 50 Hz). Further, noise is added in terms of zero-mean Gaussian-distributed random white noise to imitate the variability of source radiation effects. The standard deviation of the Gaussian noise is empirically derived from the analysis of the average deviation from the model over numerous recordings at a particular sensor location. Our synthetic input stress drop is structured as follows:

(1) A checkerboard distribution of two values, 1 and 5 MPa, varying in one degree longitude and half a degree latitude steps.
(2) We impose a depth dependence of the form $D[km]/15$ and a 1-D velocity model on top of the checkerboard distribution.
(3) We convolve the corresponding ω^{-2} spectra with a frequency-dependent attenuation function of the form $Q(f) = 300f^{0.3}$.
(4) There is no magnitude dependence in the input stress drop values.
(5) All spectra are convolved with the real data receiver terms and constant κ of the form $\kappa = 0.04f^{(0.3\,-\,1)}$, such that the whole-path attenuation is frequency dependent.
(6) Geometrical spreading is modelled using a three-part decay function $(1/r)^{\lambda_i}$. The regime change distances are R1 = 70 km and R2 = 100 km. Up to 70 km the decay exponent is $\lambda_1 = 1.0$, between 70 and 100 km, it is $\lambda_2 = 0.0$ and over 100 km, it is $\lambda_3 = 0.5$. This model accounts for the emergence of the S_MS reflection between 70 and 100 km, and the S_n refraction beyond 100 km in Switzerland (see, e.g. Deichmann *et al.* 1986; Gajewski & Prodehl 1987).

We process the synthetic data with both methods in the same fashion than the real data using the same processing parameters. We then compare the output of both methods with the synthetic input to obtain an understanding of possible bias and trade-off, as well as to get an estimate of the uncertainties inherent to both methods.

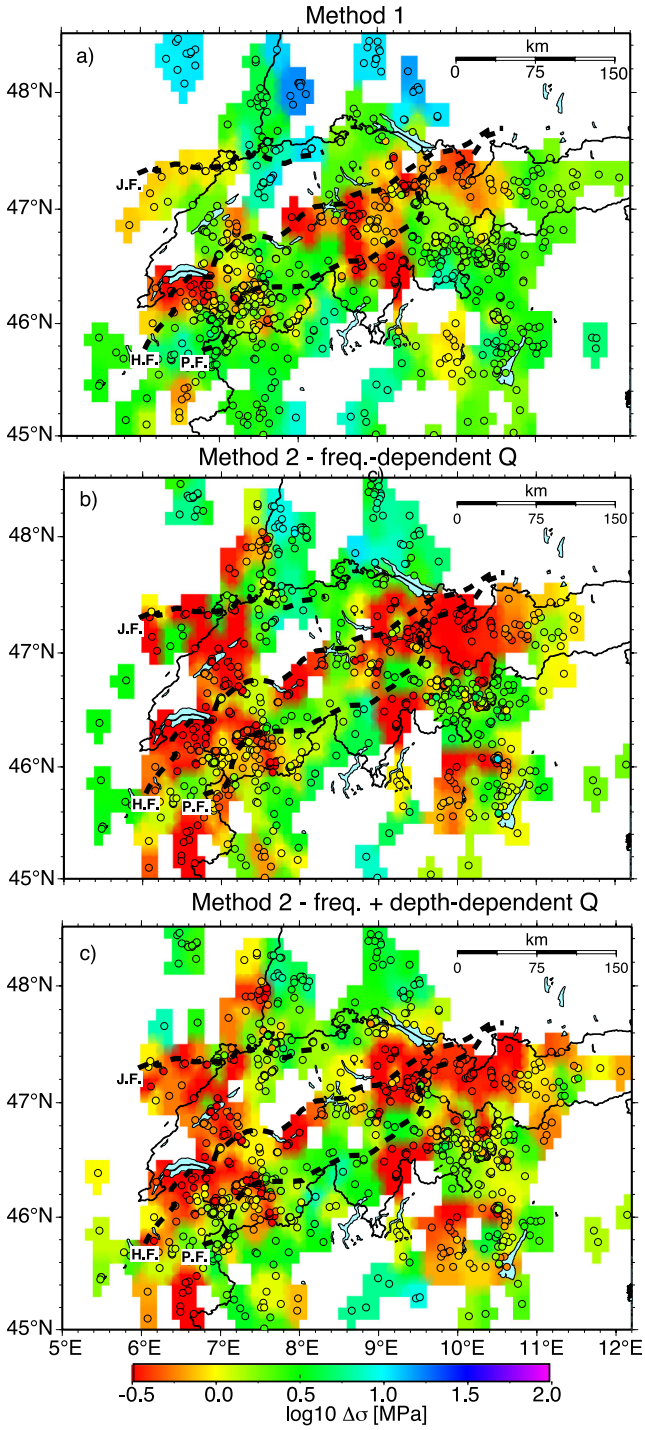

Figure 16. Lateral variations of stress drop for (a) Method 1, (b) Method 2 using a constant Q model and (c) Method 2 using a depth-dependent Q model. The main Alpine faults are shown by the bold-dashed lines (J.F., Jura front; H.F., Helvetic front; P.F., Penninic front).

Fig. 10 shows that the synthetic input is generally well resolved using both processing methods. However, as with the real data, enforcing a frequency-independent Q model in Method 2 again underestimates stress drops, whereas the frequency-dependent modelin Method 2 as well as Method 1 are able to correctly determine the input values without bias. A more quantitative comparison of the inversion results for the different methods is shown in Fig. 11. We can resolve input corner frequencies using Method 1 and Method 2 with a frequency-dependent Q model (Figs 11a and c) but we underestimate f_c using the frequency-independent Q model in Method 2 (Fig. 11b). A comparison of inverted magnitude and synthetic input magnitude also reveals an interesting dependence on the processing method (right columns in Fig. 11). As expected, Method 1 underestimates M_w at the larger magnitudes ($M_w > 3.5$) due to the fixed window length and consequent minimum frequency used in the processing (saturation). This bias in magnitudes can cause a slight underestimation of stress drops despite unbiased corner frequency estimates (Fig. 12). On the other hand, using a frequency-independent Q model in Method 2 introduces a systematic overestimation of magnitude spanning the entire magnitude range (right column in Fig. 11b). Comparing this synthetic result with the magnitude scaling of the real data for both methods (Fig. 2), we can infer that the cause for the slightly different scaling between Ω_0 of Method 1 and M_w estimated by Edwards *et al.* (2010) can be explained by a frequency-independent Q model used for their moment magnitude estimation. This observation may affect scaling between M_L and M_w (see, e.g. Goertz-Allmann *et al.* 2011a). However, the slight difference in the observed scaling of Fig. 2 is not critical for the purpose of this study. It does not have an impact on stress drop estimates of Method 1 since we only apply a constant shift to the relative magnitude estimates of Method 1, but we do not modify the observed difference in the slope.

Finally, using a frequency-dependent Q model in Method 2 inverts the input magnitudes almost exactly (right side of Fig. 11c). The results from this synthetic inversion are consistent with the real data observations and provide additional evidence that a frequency-dependent Q model may better describe our data.

A two-parametric grid search to the traveltime terms of Method 1 between 1 and 20 Hz (Fig. 13) is performed in the same manner as for the real data. Again this reveals a trade-off between the intercept Q_0 and the fall-off rate, which is shown by the 5 and 10 per cent error contours. However, the synthetic input attenuation model is well resolved and for the synthetic data inversion a frequency-independent model could be rejected within the error bounds, as opposed to the real data (Fig. 8).

Both methods are able to resolve lateral source parameter variations in a checkerboard fashion. We note, however, that the data need to be corrected for its depth dependence before the resolution of the checkerboards can be investigated. This is necessary because of strong lateral variation in maximum hypocentral depth across Switzerland, and has to be kept in mind when attempting to interpret lateral variations of the real data. Fig. 14 shows a comparison between depth-corrected synthetic input stress drop and inverted output stress drop using both methods. No spatial bias is observed that could be attributed to the given source–receiver geometry. The lateral resolution of the checkerboards is sufficiently good over the entire region of investigation.

6 LATERAL STRESS DROP VARIATIONS

Returning to the real data, we investigate the lateral variation in stress drop. Before this, however, we need to investigate a possible depth dependence of stress drop as it may affect our ability to resolve lateral variations. We know that the focal depths of earthquakes in Switzerland are not evenly distributed. The maximum hypocentral depth exhibits strong lateral variations with deeper events in the North and shallower events in the South beneath the Alps (e.g. Deichmann 1992; Deichmann *et al.* 2000). For this reason, any depth dependency of stress drops may bias any lateral variations,

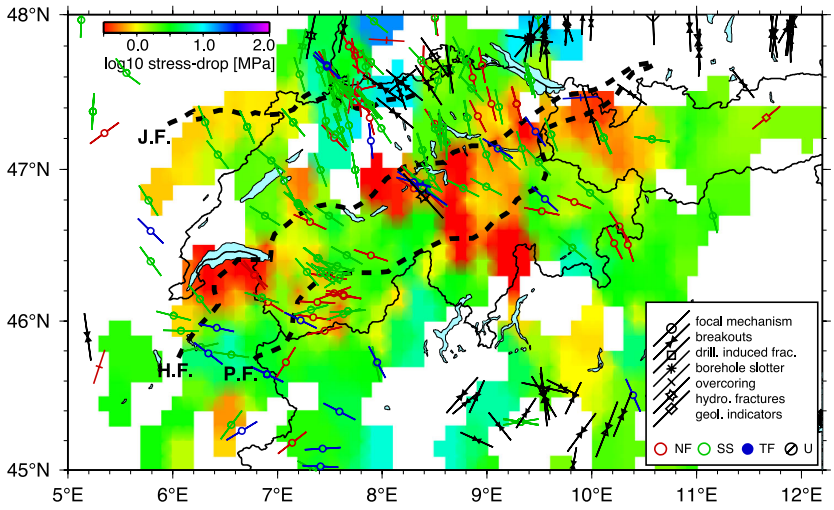

Figure 17. World Stress Map for Switzerland (from www.world-stress-map.org) compared to lateral stress drop variation using Method 1. The main Alpine faults are shown by the bold-dashed lines (J.F., Jura front; H.F., Helvetic front; P.F., Penninic front).

and we need to first correct for a depth dependence before being able to investigate lateral variations.

Previously, an apparent depth dependence of stress drop of the Parkfield seismicity could be explained with an increase of shear wave velocity in the shallow crust (Allmann & Shearer 2007), where a 1-D shear wave velocity model was used in eq. (3) rather than a constant β. Since stress drop varies as a power of three with β, the assumption of a constant β likely biases stress drop estimates in the crust. On the other hand, β of eq. (3) also scales with the rupture velocity, and, therefore, a varying shear wave velocity implies that we assume the rupture velocity to vary with depth.

Stress drops obtained from Method 1 show a strong depth dependence over more than an order of magnitude (Fig. 15a) despite being scaled with a local shear wave velocity from 3-D tomographic models (Husen *et al.* 2003; Diehl *et al.* 2005). Deeper events below 20 km show a higher mean stress drop with reduced scatter. Focal depth variations of source parameters in Switzerland have been found previously by Spada *et al.* (2013). They find a linear decrease of *b*-value with depth between about 0 and 20 km in the Alpine foreland and link this to an increase in differential stress with depth. The increase in differential stress may also explain our observed increase in stress drop with depth (Goertz-Allmann & Wiemer 2013). Using a frequency-dependent, but depth-invariant $Q(f)$ function in Method 2 shows a similar depth dependence of stress drop (Fig. 15b). However, when assuming Q to depend both on depth and frequency, $Q(f, z)$ in Method 2 (Fig. 15c), we observe that the depth dependence of stress drop disappears. For this case, the variation of the median stress drop values is within the error bars obtained from bootstrap resampling. We can, therefore, explain an increasing stress drop with depth equally well by decreasing attenuation (increasing Q) with depth. Note also that uncertainties in earthquake depth are usually large. Depending on the location method and number of traces used to estimate the depth, the uncertainty is typically a few kilometres for the Swiss catalogue but may be as large as $\pm$10 km in worse cases. In our study, we use the available catalogue depth, however, a refined determination of the hypocentral depth of all events could reveal further details of the lateral variations discussed below.

Last but not least, we now investigate and interpret lateral variations in Brune stress drop across Switzerland. Fig. 16 shows stress drop estimates projected onto individual event location and interpolated by applying a median filter over the closest four events. We observe significant lateral variations of stress drop: areas of relatively higher stress drop are concentrated to the North and the South, for example, in the area around Basel, the Rhine graben and North of Lake Constance. The most striking feature is a lower stress drop band following the northern edge of the Alpine deformation front. This relative pattern of low and high stress drops is very stable and does not change by a modification of processing parameters or between the two different processing methods. In fact, we still observe the same pattern when assuming a depth-independent Q in Method 2 (Fig. 16b).

The isolated source spectra obtained using Method 1 may still contain some near-source attenuation, which cannot be separated easily from the source. One possibility to correct for near-source attenuation is to use a spatially varying empirical correction as in Allmann & Shearer (2007). However, the event population in Switzerland is too sparse to apply this approach. The observed lateral stress drop variations may, therefore, also be affected by so far unaccounted lateral variations in attenuation near the source. Unfortunately, a 3-D model of intrinsic attenuation does not yet exist for Switzerland. Such a model could be inverted using a tomographic approach (see, e.g. Schurr *et al.* 2003; Edwards *et al.* 2008).

In any case, the robust relative lateral variations that we observe with both methods show a band of lower stress drop values along the main Alpine deformation front (front of the Helvetic nappe, Fig. 16). It may be possible that the observed band of low stress drops could either be associated with higher pore pressures along the thrust fronts, or it could be a sign for variations in differential stress. Coupling stress drop to differential stress can explain observed stress drop reductions in the presence of strong pore pressure increases during a hydraulic stimulation (Goertz-Allmann *et al.* 2011b; Goertz-Allmann & Wiemer 2013). On the other hand, different faulting regimes have different levels of differential stress, which gives rise to variations in *b*-value (Schorlemmer & Wiemer 2005). For this reason, we compare our stress drop results with the stress orientations in Switzerland obtained from the World Stress Map (Fig. 17, Heidbach *et al.* 2008). Many data points in the swiss part of the World Stress Map stem from moment tensor inversions of Kastrup *et al.* (2004), which includes some of the events of our

study. Moment tensor inversion for central Switzerland indicate a dominance of strike-slip events, as can be seen on the World Stress Map for Switzerland (Fig. 17). However, there is no clear regional clustering of the present-day stress regimes that would facilitate a comparison with the stress drop results. Therefore, we see no obvious correlation of stress drop values with faulting regime that would point to a connection between stress drop and differential stress. However, the lack of correlation can also partly be explained by the very uneven distribution of stress data, as well as by the very heterogeneous distribution of present-day stress regimes in Switzerland. Despite the lack of direct correlation with stress orientation in Fig. 17, a visual correlation of low stress drop with the main deformation fronts is evident, and, therefore, we speculate that some tectonic causes must be at play to produce the observed stress drop patterns.

7 CONCLUSIONS

We estimate source properties of small to moderate earthquakes in Switzerland from isolated source spectra using two independent spectral analysis methods, a data-driven method and a model-dependent method. An initial discrepancy of absolute stress drop values between the two methods can be attributed to a trade-off between attenuation and source and provides evidence for a frequency-dependent attenuation in Switzerland. This evidence is further affirmed by results of a synthetic test.

Despite the high scatter in individual stress drop estimates, robust features in the data show (1) an increase of stress drop with hypocentral depth, which may also be explained by a decrease of attenuation with depth, and (2) lateral variations of stress drop with higher values in northern Switzerland and lower values along the Alpine deformation front. However, we do not see an obvious correlation of our stress drop results with stress orientations in Switzerland. The latter would be evidence for a relation between stress drop and differential stress.

An important aspect for seismic hazard assessment in Switzerland is the question about scaling between small and large earthquakes. While we cannot exclude the possibility of a non-constant scaling relation, we find that our data do not provide sufficient evidence of such a scaling and the possible causes of bias are too large.

ACKNOWLEDGEMENTS

This research was supported in part by the Swiss Federal Nuclear Safety Inspectorate (ENSI). We are grateful to Alex Goertz and Nicholas Deichmann for fruitful discussions. Two anonymous reviewers are acknowledged for providing feedback that helped improving the manuscript.

REFERENCES

Abercrombie, R., 1995. Earthquake source scaling relationships from −1 to $5M_L$ using seismograms recorded at 2.5 km depth, *J. geophys. Res.,* **100,** 24 015–24 036.

Abercrombie, R., 2000. Crustal attenuation and site effects at Parkfield, California, *J. geophys. Res.,* **105**(B3), 6277–6286.

Adams, D. & Abercrombie, R., 1998. Seismic attenuation above 10 Hz in southern California from coda waves recorded in the Cajon Pass borehole, *J. geophys. Res.,* **103**(B10), 24 257–24 270.

Allmann, B. & Shearer, P., 2007. Spatial and temporal stress drop variations in small earthquakes near Parkfield California, *J. geophys. Res.,* **112,** B04305, doi:10.1029/2006JB004395.

Allmann, B. & Shearer, P., 2009. Global variations of stress drop for moderate to large earthquakes, *J. geophys. Res.,* **114,** B01310, doi:10.1029/2008JB005821.

Anderson, J. & Hough, S., 1984. A model for the shape of the F fourier amplitude spectrum of acceleration at high-frequencies, *Bull. seism. Soc. Am.,* **74**(5), 1969–1993.

Archuleta, R., Cranswick, E., Mueller, C. & Spudich, P., 1982. Source parameters of the 1980 Mammoth Lakes, California, earthquake sequence, *J. geophys. Res.,* **87,** 4595–4607.

Blias, E., 2012. Accurate interval q-factor estimation from vsp data, *Geophysics,* **77**(3), WA149–WA156.

Braunmiller, J., Deichmann, N., Giardini, D. & Wiemer, S. the SED Magnitude Working Group, 2005. Homogeneous moment-magnitude calibration in Switzerland, *Bull. seism. Soc. Am.,* **95,** 58–74.

Brune, J., 1970. Tectonic stress and spectra of seismic shear waves from earthquakes, *J. geophys. Res.,* **75,** 4997–5009.

Brune, J., 1971. Correction: tectonic stress and spectra of seismic shear waves from earthquakes, *J. geophys. Res.,* **76,** 5002.

Castro, R., Anderson, J. & Singh, S., 1990. Site response, attenuation and source spectra of S-waves along the Guerrero, Mexico, subduction zone, *Bull. seism. Soc. Am.,* **80**(6), 1481–1503.

Deichmann, N., 1992. Structural and rheological implications of lower-crustal earthquakes below northern Switzerland, *Phys. Earth planet. Inter.,* **69,** 270–280.

Deichmann, N. & Ernst, J., 2009. Earthquake focal mechanisms of the induced seismicity in 2006 and 2007 below Basel (Switzerland), *Swiss J. Geosci.,* **102**(3), 457–466.

Deichmann, N., Ansorge, J. & Mueller, S., 1986. Crustal structure of the southern Alps beneath the intersection with the European geotraverse, *Tectonophysics,* **126,** 57–83.

Deichmann, N. *et al.*, 2000. Earthquakes in Switzerland and surrounding regions during 1999, *Eclogae Geologicae Helvetiae,* **93**(3), 395–406.

Diehl, T., Deichmann, N., Husen, S. & Kissling, E., 2005. Assessment of quality and consistency of S-wave arrivals in local earthquake data., Abstract, in *Geophysical Research Abstracts*, Vol. **7,** 04912, EGU.

Diehl, T., Deichmann, N., Kissling, E. & Husen, S., 2009. Automatic S-wave picker for local earthquake tomography, *Bull. seism. Soc. Am.,* **99**(3), 1906–1920.

Drouet, S., Chevrot, S., Cotton, F. & Souriau, A., 2008. Simultaneous inversion of source spectra, attenuation parameters, and site response: application to the data of the French accelerometric network, *Bull. seism. Soc. Am.,* **98**(1), 198–219.

Edwards, B. & Fäh, D., 2013. A stochastic ground-motion model for Switzerland, *Bull. seism. Soc. Am.,* **103**(1), 78–98.

Edwards, B. & Rietbrock, A., 2009. A comparative study on attenuation and source-scaling relations in the Kanto, Tokai, and Chubu regions of Japan, using data from Hi-Net and Kik-Net, *Bull. seism. Soc. Am.,* **99,** doi:10.1785/0120080292.

Edwards, B., Rietbrock, A., Bommer, J. & Baptie, B., 2008. The acquisition of source, path and site effects from micro-earthquake recordings using Q tomography: application to the UK, *Bull. seism. Soc. Am.,* **98,** 1915–1935.

Edwards, B., Allmann, B., Fäh, D. & Clinton., J., 2010. Automatic computation of moment magnitudes for small earthquakes and the scaling of local to moment magnitude, *Geophys. J. Int.,* **183,** 407–420.

Edwards, B., Fäh, D. & Giardini, D., 2011. Attenuation of seismic shear wave energy in Switzerland, *Geophys. J. Int.,* **185**(2), 967–984.

Eshelby, J., 1957. The determination of the elastic field of an ellipsoidal inclusion, and related problems, *Proc. R. S. A,* **241**(1226), 376–396.

Gajewski, D. & Prodehl, C., 1987. Seismic refraction investigation of the Black Forest, *Tectonophysics,* **142,** 27–48.

Gibowicz, S.J., Young, R.P., Talebi, S. & Rawlence, D.J., 1991. Source parameters of seismic events at the Underground Research Laboratory in Manitoba, Canada: scaling relations for events with moment magnitude smaller than -2, *Bull. seism. Soc. Am.,* **81**(4), 1157–1182.

Goertz-Allmann, B.P. & Wiemer, S., 2013. Geomechanical modeling of induced seismicity source parameters and implications for seismic hazard assessment, *Geophysics,* **78**(1), KS25–KS39.

Goertz-Allmann, B.P., Edwards, B., Bethmann, F., Deichmann, N., Clinton, J., Fah, D. & Giardini, D., 2011a. A new empirical magnitude scaling relation for Switzerland, *Bull. seism. Soc. Am.,* **101**(6), 3088–3095.

Goertz-Allmann, B.P., Goertz, A. & Wiemer, S., 2011b. Stress drop variations of induced earthquakes at the Basel geothermal site, *Geophys. Res. Lett.,* **38**(9), L09308, doi: 10.1029/2011GL047498.

Haskell, N., 1964. Total energy and energy spectral density of elastic wave radiation from propagating faults, *Bull. seism. Soc. Am.,* **54,** 1811–1841.

Heidbach, O., Tingay, M., Barth, A., Reinecker, J., Kurfess, D. & Müller, B., 2008. *The World Stress Map database release (2008),* doi:10.1594/GFZ.WSM.Rel2008.

Hough, S., 1997. Empirical Green's function analysis: taking the next step, *J. geophys. Res.,* **102,** 5369–5384.

Hough, S. & Anderson, J., 1988. High-frequency spectra observed at Anza, California: implications for Q structure, *Bull. seism. Soc. Am.,* **78,** 692–707.

Husen, S., Kissling, E., Deichmann, N., Wiemer, S., Giardini, D. & Baer, M., 2003. Probabilistic earthquake location in complex three-dimensional velocity models: application to Switzerland, *J. geophys. Res.,* **108**(B2), 2077, doi:10.1029/2002JB001778.

Ide, S. & Beroza, G., 2001. Does apparent stress vary with earthquake size?, *Geophys. Res. Lett.,* **28,** 3349–3352.

Ide, S., Beroza, G., Prejean, S. & Ellsworth, W., 2003. Apparent break in earthquake scaling due to path and site effects on deep borehole recordings, *J. geophys. Res.,* **108**(B5), 2271, doi:10.1029/2001JB001617.

Jost, M.L., Büsselberg, T., Jost, O. & Harjes, H.-P., 1998. Source parameters of injection-induced microearthquakes at 9 km depth at the KTB deep drilling site, Germany, *Bull. seism. Soc. Am.,* **88**(3), 815–832.

Kanamori, H., Jennings, P., Singh, S. & Astiz, L., 1993. Estimation of strong ground motions in Mexico-City expected for large earthquakes in the Guerrero seismic gap, *Bull. seism. Soc. Am.,* **83**(3), 811–829.

Kane, D., Shearer, P., Goertz-Allmann, B. & Vernon, F., 2013. Rupture directivity of small earthquakes at Parkfield, *J. geophys. Res.,* **118**(1), 212–221.

Kastrup, U., Zoback, M., Deichmann, N., Evans, K., Giardini, D. & Michael, A., 2004. Stress field variations in the Swiss Alps and the northern Alpine foreland derived from inversion of fault plane solutions, *J. geophys. Res.,* **109**(B1), B01402, doi:10.1029/2003JB002550.

Lees, J.M. & Park, J., 1995. Multiple-taper spectral analysis: a stand-alone C subroutine, *Comput. Geosci.,* **21,** 199–236.

Madariaga, R., 1976. Dynamics of an expanding circular fault, *Bull. seism. Soc. Am.,* **66,** 639–666.

Madariaga, R., 1977. High-frequency radiation from crack (stress drop) models of earthquake faulting, *Geophys. J. R. astr. Soc,* **51,** 625–651.

Mayeda, K. & Walter, W.R., 1996. Moment, energy, stress drop, and source spectra of western United States earthquakes from regional coda envelopes, *J. geophys. Res.,* **101**(B5), 11 195–11 208.

McNamara, D. *et al.*, 2012. Frequency-dependent seismic attenuation within the Hisaniola island region of the Caribbean sea, *Bull. seism. Soc. Am.,* **102**(2), 773–782.

Morozov, I., Zhang, C., Duenow, J., Morozova, E. & Smithson, S., 2008. Frequency dependence of coda Q, part I: numerical modeling and examples from peaceful nuclear explosions, *Bull. seism. Soc. Am.,* **98,** 2615–2628.

Mueller, C., 1985. Source pulse enhancement by deconvolution of an empirical Green's function, *Geophys. Res. Lett.,* **12,** 33–36.

Oth, A., Bindi, D., Parolai, S. & Giacomo, D.D., 2011. Spectral analysis of K-NET and KiK-net data in Japan, Part II: on attenuation characteristics, source spectra, and site response of borehole and surface stations, *Bull. seism. Soc. Am.,* **101**(2), 667–687.

Park, J., Lindberg, C. & Vernon, F., 1987. Multitaper spectral analysis of high–frequency seismograms, *J. geophys. Res.,* **92,** 12 675–12 648.

Prejean, S. & Ellsworth, W., 2001. Observations of earthquake source parameters at 2 km depth in the Long Valley Caldera, Eastern California, *Bull. seism. Soc. Am.,* **91,** 165–177.

Prieto, G.A., Parker, R.L. & Vernon, F.L., 2009. A Fortran 90 library for multitaper spectrum analysis, *Comput. Geosci.,* **35,** 1701–1710.

Schorlemmer, D. & Wiemer, S., 2005. Microseismicity data forecast rupture area, *Nature,* **434,** 1086, doi:10.1038/4341086a.

Schurr, B., Asch, G., Rietbrock, A., Trumbull, R. & Haberland, C., 2003. Complex patterns of fluid and melt transport in the central Andean subduction zone revealed by attenuation tomography, *Earth planet. Sci. Lett.,* **215**(1–2), 105–119.

Shearer, P., Prieto, G. & Hauksson, E., 2006. Comprehensive analysis of earthquake source spectra in southern California, *J. geophys. Res.,* **111,** B06303, doi:10.1029/2005JB003979.

Spada, M., Tormann, T., Wiemer, S. & Enescu, B., 2013. Generic dependence of the frequency-size distribution of earthquakes on depth and its relation to the strength profile of the crust, *Geophys. Res. Lett.,* **40**(4), 709–714.

Toverud, T. & Ursin, B., 2005. Comparison of seismic attenuation models using zero-offset vertical seismic profiling (VSP) data, *Geophysics,* **70**(2), F17–F25.

Viegas, G., Abercrombie, R. & Kim, W.-Y., 2010. The 2002 M5 Au Sable Forks, NY, earthquake sequence: source scaling relationships and energy budget, *J. geophys. Res.,* **115,** B07310, doi:10.1029/2009JB006799.